Journal of Applied Physics

RESEARCH ARTICLE | JANUARY 19 2022

Non-equilibrium plasma generation via nano-second multi-mode laser pulses FREE

Andrea Alberti ; Alessandro Munafò ; Munetake Nishihara; Carlos Pantano; Jonathan B. Freund; Marco Panesi

Check for updates

Journal of Applied Physics 131, 033102 (2022)
https://doi.org/10.1063/5.0065999
CHORUS

View Online
Export Citation
CrossMark

Articles You May Be Interested In

Calculation of the heat flux and pressure on the double cone surface in a high-enthalpy non-equilibrium air flow

AIP Conference Proceedings (July 2019)

Calculation of the heat flux and pressure on the cone surface in a high-enthalpy non-equilibrium flow of a binary nitrogen mixture (N_2/N)

AIP Conference Proceedings (November 2018)

Thermochemical nonequilibrium effects on high-enthalpy double-wedge flows

Physics of Fluids (June 2022)

30 August 2023 12:22:34

AIP Publishing

Journal of Applied Physics ARTICLE scitation.org/journal/jap

Non-equilibrium plasma generation via nano-second multi-mode laser pulses

Cite as: J. Appl. Phys. **131**, 033102 (2022); doi: 10.1063/5.0065999
Submitted: 6 August 2021 · Accepted: 22 December 2021 ·
Published Online: 19 January 2022

View Online Export Citation CrossMark

Andrea Alberti,[1,2] Alessandro Munafò,[1,2] Munetake Nishihara,[1] Carlos Pantano,[1,3] Jonathan B. Freund,[1,2,3] and Marco Panesi[1,2,a)]

AFFILIATIONS

[1]The Center for Exascale Simulation of Plasma-coupled Combustion, University of Illinois at Urbana-Champaign, 1308 W. Main St., Urbana, Illinois 61801, USA
[2]Department of Aerospace Engineering, University of Illinois at Urbana-Champaign, 104 S. Wright St., Urbana, Illinois 61801, USA
[3]Department of Mechanical Science and Engineering, University of Illinois at Urbana-Champaign, 1206 W. Green St., Urbana, Illinois 61801, USA

[a)]**Author to whom correspondence should be addressed:** mpanesi@illinois.edu

ABSTRACT

The formation and growth of plasma kernels generated via nano-second mode-beating laser pulses is investigated here via a non-equilibrium self-consistent computational model. Chemically reactive Navier–Stokes equations are used to describe the hydrodynamics, and non-equilibrium effects are taken into account with a two-temperature model. Inverse Bremsstrahlung and multiphoton ionization are included self-consistently in the model via a coupled solution of the plasma governing equations and the radiative transfer equation (that describes the laser beam propagation and attenuation). A self-consistent approach (despite carrying additional challenges) minimizes the empiricism and it allows for a more accurate description since it prevents both the utilization of artificial plasma seeds to trigger the breakdown and the implementation of tuning parameters to simulate the laser-energy deposition. The advantages of this approach are confirmed by the good agreement between the numerically predicted and the experimentally measured plasma boundary evolution and absorbed energy. This also holds true for the periodic plasma kernel structures that, as suggested by the experiments and confirmed by the simulations presented here, are connected to the modulating frequency.

Published under an exclusive license by AIP Publishing. https://doi.org/10.1063/5.0065999

30 August 2023 12:22:34

I. INTRODUCTION

The first studies on the optical breakdown of gases began in the 1960s with the advent of powerful Q-switched lasers.[1–5] Many applications have been extensively investigated, including laser-induced ignition,[6–14] flow control,[15–27] laser ablation,[28] and spectroscopy.[29,30]

Breakdown is observed when a laser beam of sufficient intensity is focused onto a gas (e.g., air) which is normally transparent to optical radiation.[1–5,31] Investigators were initially a bit puzzled by this finding as they were unable to justify the breakdown on a theoretical basis. It was soon recognized that the disagreement between theory and experiments was caused by the reliance of the former on linear optics. As a matter of fact, for the large intensities attainable by Q-switched lasers, non-linear processes, such as multiphoton ionization (MPI), produce cold *priming* electrons which, upon draining energy from the beam via inverse Bremsstrahlung (IB), may trigger a cascade ionization process. This mechanism of plasma formation has been confirmed by both experiments and calculations. For a given gas, a breakdown is not observed below a threshold intensity. The value of the former depends on several factors, such as ambient conditions (e.g., pressure and temperature), beam wavelength, and optics of the focusing system (e.g., focal length), and is also affected by the presence of impurities (e.g., aerosols) and trace gases with low ionization potential.

The final outcome of laser-induced breakdown (LIB) is the formation of a transient high-temperature and strongly ionized plasma. For nano-second pulses considered here, maximum temperatures of the order of 10^5 up to 10^6 K are to be expected during the discharge. This conclusion was first reached independently by both De Michelis,[32] who concentrated on LIB in atmospheric air (using a ruby laser $h_P\nu = 1.78$ eV), and by Zel'dovich and Raizer.[33,34] These estimates have been corroborated by both

Published under an exclusive license by AIP Publishing

experiments and calculations. For instance, in the work by Bradley *et al.*,[35] where a Q-switched Nd:YAG laser was used to promote breakdown in both air and isooctane–air mixtures, free-electron temperatures above 10^5 K were inferred based on the blast-wave theory. Other authors, such as Phuoc and White,[36] report temperatures larger than 10^5 K. The writers of this paper[37–39] performed physics based numerical simulations, which led to peak temperatures around 5×10^5 K. After the discharge, the plasma expands and propagates through the ambient gas. This is accompanied by a significant temperature decrease as a result of the conservation of energy and growth of the front of the laser-induced blast wave. With time, the latter degenerates into an approximately spherical sound wave. A typical temperature vs time evolution plot for a nano-second laser discharge is shown in Fig. 1. There, the values from Harilal *et al.*[40] (who fitted spark temperature behind the shock wave data by Zel'dovich and Raizer; Harilal *et al.* use a 1 064 nm pulse at 55 mJ from a Q-switched Nd:YAG laser Continuum Surelite II with a duration of 6 ns FWHM, and a focal spot size of 10 μm) are extrapolated into discharge phase and compared with the maximum temperatures predicted by the authors at $t = 5$ ns for LIB in air. The overall agreement is good and further confirms the above figures on temperature values to be expected during the discharge phase.

Modeling of LIB in gases is a complex multi-physics problem, requiring a self-consistent coupled solution of the equations governing hydrodynamics and radiation. Under most situations, the gas onto which the laser is focused is collision dominated and, in light of this, may be treated using a fluid description (e.g., Navier–Stokes equations). Emission, absorption, and scattering of light are taken into account via the Radiative Transfer Equation (RTE), which is the equivalent of Boltzmann's equation for a photon gas[41] (see the Appendix). The inclusion of finite-rate (i.e., non-equilibrium) collisional and radiative processes (e.g., ionization, absorption) is accomplished by means of either multi-temperature[37–39,42–45] or state-to-state models.[29,46] For CFD (Computational Fluid Dynamics) applications, the former is often the preferred choice due to the large computational cost associated to tracking the population of hundreds to thousands atomic/molecular *bound* states as required by a state-to-state approach.

In their previous works, the authors developed and validated a predictive LIB model where the RTE, which accounted for attenuation and propagation of the laser beam, is coupled to the Navier–Stokes equations for a multi-component plasma.[37–39,47] In this computational framework, non-equilibrium phenomena are taken into account via a two-temperature model (though state-to-state models may be also used in light of a general and flexible implementation). As opposed to what is usually done in the literature,[42–45,48,49] both multiphoton ionization (MPI) and inverse Bremsstrahlung (IB) are self-consistently coupled with the hydrodynamics. This avoids using an initial artificial plasma and, more importantly, was crucial in reproducing the experimentally observed plasma kernel dynamics. In particular, during the plasma formation, MPI is the guiding process of the plasma waves. This is opposed to the common view according to which MPI is considered important only at early times for the production of *priming* electrons (e.g., around pico-second timescales) and becomes negligible thereafter. The LIB model developed by the authors has been extensively validated for single-mode pulses (e.g., Gaussian time evolution) for a broad range of beam energy and wavelength, and ambient conditions. Overall good agreement with experiments has been reported for both the discharge[38] and the post-discharge phases.[39]

During the discharge, spatially periodic plasma kernel structures are observed for both femto-second and nano-second pulses in both single- and multi-mode configurations.[50–53] Moreover, for multi-mode lasers, an enhancement of electrons produced via MPI has also been predicted[54] and observed.[55] Several mechanisms have been proposed for describing the onset and dynamics of the periodic structures, such as self-focusing,[56] lens aberration,[57] and hydrodynamic instabilities.[58] For instance, for short pulses (e.g., 10^{13} W/cm^2) self-focusing has been confirmed as the primary mechanism,[59] but these structures are also observed at lower intensities of nano-second discharges. Nishihara *et al.*[50] reported that the spatial wavelength between the periodic structures seems to agree with hydrodynamic instabilities generated by the interaction at the plasma surface between excited and transmitted plasma *waves*. It has been suggested that lateral radiative heat flux in the breakdown region and the rapid plasma expansion combined together might result in inhomogeneous refraction, which can then produce periodic structures.[58] The period in this case would depend on the laser wavelength and the angle of inclination of the Bessel beam.[58] However, Nishihara *et al.*[50] observed that the periodic structure of the electron density distribution was related to the laser mode-beating frequency, suggesting that the multi-mode

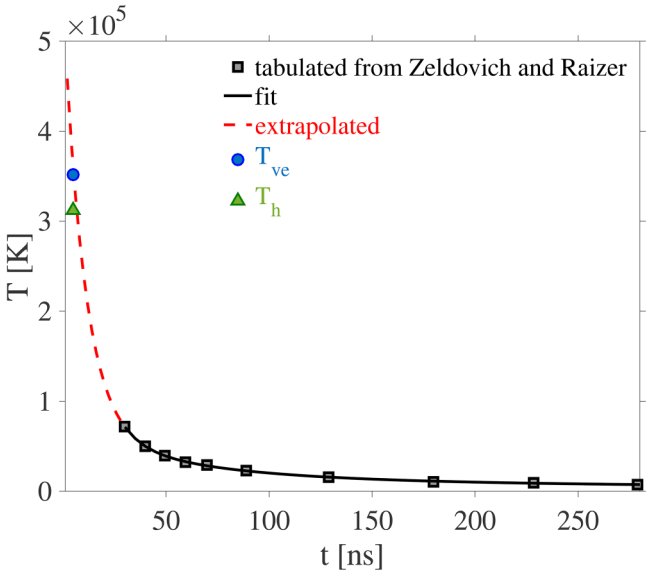

FIG. 1. Evolution of spark temperature during breakdown and post-breakdown stages: maximum free-electron vibronic (T_{ve}) and heavy-particle (T_h) temperatures predicted by the authors for case 2 (see Sec. III C) at 5 ns into the discharge (circle and triangle, respectively), the temperature behind the shock wave reported by Harilal *et al.*[40] (square symbol, tabulated values from Zeldovich and Raizer), curve-fit of Harilal *et al.* in the post-discharge phase (solid black line), and extrapolation of the curve-fit into the discharge phase (red broken line).

30 August 2023 12:22:34

Published under an exclusive license by AIP Publishing

pulse either seeds instabilities or directly generates periodic kernel structures that match the beating mode.

The purpose of this work is to investigate the generation mechanism of plasma periodic structures observed in multi-mode nano-second pulses[50] by means of the self-consistent LIB model developed by the authors.[37–39]

This paper is structured as follows. Section II describes the physical model and the numerical method. In Sec. III, the results for multi-mode LIB in air are first compared against experiments for validation. This is followed by an in-depth analysis of the generation mechanism of the plasma periodic structures. Conclusions are summarized in Sec. IV.

II. PHYSICAL MODEL AND NUMERICAL METHOD

The gas onto which the laser is focused is air made of 79 % N_2 and 21 % O_2 at ambient conditions. The laser-induced plasma is modeled as a mixture of ideal gases (e.g., no pressure ionization[34]) and accounts for chemical components resulting from dissociation and ionization of molecular nitrogen and oxygen,

$$\mathcal{S} = \{e^-,\ N,\ O,\ N_2,\ O_2,\ NO,\ N^+,\ N^{2+},\ N^{3+},\ N^{4+},$$

$$N^{5+},\ O^+,\ O^{2+},\ O^{3+},\ O^{4+},\ O^{5+},\ N_2^+,\ O_2^+,\ NO^+\}.$$

Here, only positively charged ions are considered.

A. Hydrodynamics

The non-equilibrium hydrodynamics are described based on a two-temperature model, where the heavy-particle temperature, T_h, is associated with the roto-translational degrees of freedom of heavy-particles (i.e., atoms and molecules), whereas the free-electron-vibronic temperature, T_{ve}, is associated with translation of free-electrons and vibration of molecules and electronic excitation of heavy-particles. The flow governing equations are[37,60]

$$\frac{\partial \rho_s}{\partial t} + \nabla \cdot (\rho_s \mathbf{u}) = -\nabla \cdot \mathbf{J}_s + \omega_s, \quad s \in \mathcal{S}, \tag{1}$$

$$\frac{\partial \rho \mathbf{u}}{\partial t} + \nabla \cdot (\rho \mathbf{u}\mathbf{u} + p\,I) = \nabla \cdot \tau, \tag{2}$$

$$\frac{\partial \rho E}{\partial t} + \nabla \cdot (\rho H \mathbf{u}) = \nabla \cdot (\tau \mathbf{u} - \mathbf{q}) + \Omega^R, \tag{3}$$

$$\frac{\partial \rho e_{ve}}{\partial t} + \nabla \cdot (\rho e_{ve} \mathbf{u}) = -\nabla \cdot \mathbf{q}_{ve} - p_e \nabla \cdot \mathbf{u} + \Omega^C_{ve} + \Omega^R_{ve}, \tag{4}$$

where the "ve" subscript identifies quantities related to the free-electron-vibronic degrees of freedom alone. The symbols in Eqs. (1)–(4) have their usual meaning.[37–39,60] ρ_s are the partial densities, from which the gas density may be aimed via $\rho = \sum_{s\in\mathcal{S}} \rho_s$. p and p_e symbols denote, respectively,the gas and free-electron pressure. The capital letter E stands for the total energy per unit-mass. The former accounts for thermal, formation,and kinetic contributions and may be used to compute the total enthalpy based on its definition, $H = E + p/\rho$. The Greek symbols ω and Ω represent, respectively, mass and energy production terms due to collisional (C) and radiative (R) processes. The boldface quantities $\mathbf{u}$, $\mathbf{J}_s$,and $\mathbf{q}$ denote the mass-averaged velocity, the mass diffusion, and the heat flux vectors, respectively, whereas the symbols I and τ stand for the identity and viscous stress tensors, respectively. The collisional kinetic processes included in the model are dissociation by heavy-particle and electron impact, ionization by electron impact, particle exchange (e.g., Zel'dovich reactions), charge exchange, and associative ionization reactions. Details on the constitutive relations for thermodynamics, transport,and kinetics for the governing Eqs. (1)–(4) are reported elsewhere.[37,47]

B. Radiation

The evolution of the monochromatic intensity of the collimated beam, I_λ, where λ stands for its wavelength, is governed by the Radiative Transfer Equation (RTE).[41] Since the collimated radiation (i.e., the laser beam) is expected to represent the prominent role in the radiative energy transfer for the laser under investigation and since the time scales of laser pulse and hydrodynamics are much slower of light propagation, we can assume steady-state (i.e., $\partial()/\partial t = 0$) and neglect emission, scattering, and refraction. Under those assumptions, the RTE reduces to Beer–Lambert's law,

$$\mathbf{n} \cdot \nabla I_\lambda = -\kappa_\lambda I_\lambda, \tag{5}$$

where κ_λ is the monochromatic absorption coefficient corrected for stimulated emission, and $\mathbf{n}$ is the direction cosine along the line of sight.

The radiative processes taken into account are multiphoton ionization (MPI) and inverse Bremsstrahlung (IB). MPI rate coefficients are evaluated based on Morgan's formula,[2,4,61] whereas the IB absorption coefficient is computed using Kramers' formula for electron–ion interactions[34] and the model by Kroll and Watson[62] for electron–neutral interactions. More details are reported elsewhere.[37,38]

C. Numerical method

The axially symmetric form of Eqs. (1)–(4) is solved using the HEGEL plasma solver.[37] The flow governing equations are first discretized in space based on the cell-centered finite volume method. Inviscid fluxes are evaluated using van Leer's flux vector splitting in conjunction with a second-order upwind-biased MUSCL

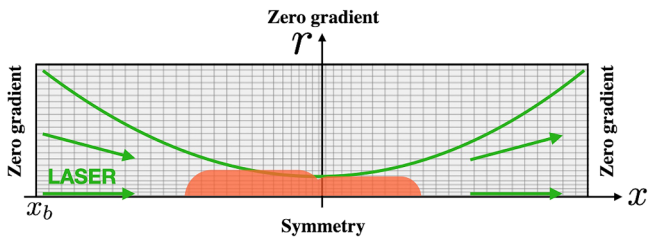

FIG. 2. Schematics of the simulation setup.

30 August 2023 12:22:34

Published under an exclusive license by AIP Publishing

TABLE I. Fit coefficients for the multi-mode waveform.

k	a_k	b_k (GHz)	c_k
1	0.845 8	0.2029	−0.141
2	0.016 16	1.121	19.08
3	0.008 364	3.569	−12.63
4	0.170 3	0.6289	−3.567
5	−0.060 75	4.081	−6.067
6	0.219	4.493	−5.947
7	0.032 29	5.355	−7.695
8	0.184 2	4.9	−9.502

reconstruction. Diffusive fluxes are computed using Green–Gauss's formula to evaluate face-averaged gradients. The spatial discretization is followed by a temporal integration accomplished via an Implicit-Explicit (IMEX) dual-time-stepping method. RTE (5) is solved based on a flux-tube formulation.[37]

III. RESULTS

The simulation setup (e.g., grid, laser beam, and focusing system parameters) for the various cases are introduced in Sec. III A. This is followed by validation via comparison against experiments in Sec. III B. Finally, the generation mechanism of plasma periodic structures is investigated in Sec. III C.

A. Simulation setup

A rectangular (axisymmetric) computational domain is discretized using a two-dimensional Cartesian structured grid along the x and r coordinates (see Fig. 2). The focal plane is taken at the origin. The beam propagates along the positive x direction.

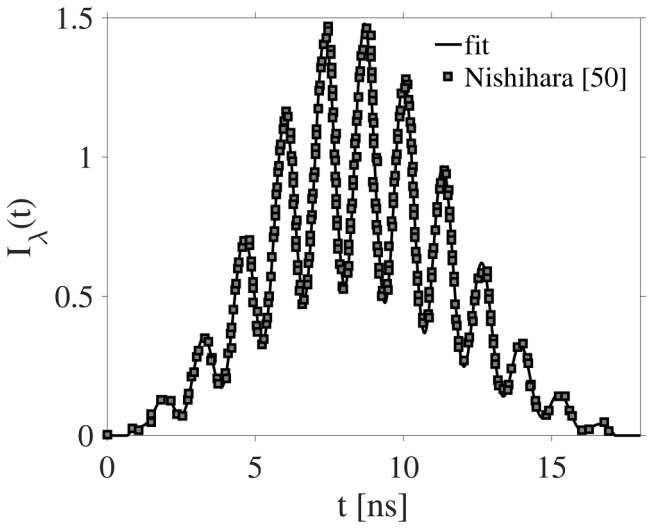

FIG. 3. Multi-mode waveform: comparison between fitting formula [i.e., bracketed term in Eq. (8)] and calculated experimental waveform of Nishihara *et al.*.[50]

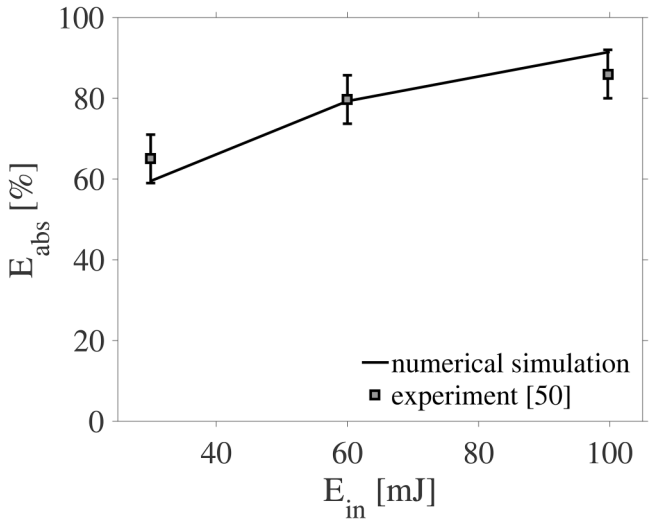

FIG. 4. Comparison between predicted and experimentally measured absorbed energy ($w_f = 7.3\,\mu$m, $f = 100$mm).

The boundary conditions for the hydrodynamic Eqs. (1)–(4) are symmetry on the optical (i.e., x) axis and zero-gradient at the other boundaries. For the laser beam, the intensity at the incoming boundary $I_\lambda(x_b, r, t)$, placed at $x = x_b < 0$, is prescribed as

$$I_\lambda = I_0 \exp\left(-\frac{r^2}{2\sigma_r^2}\right) g_{mb}(t) \exp\left[-\frac{(t - t_p/2)^2}{2\sigma_t^2}\right], \quad (6)$$

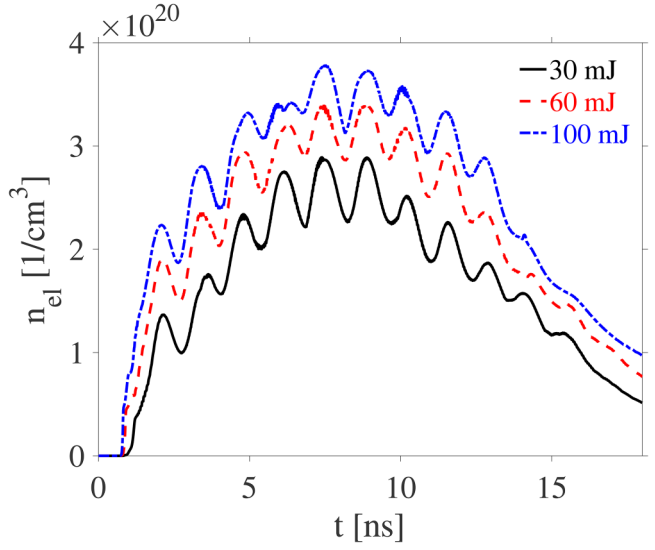

FIG. 5. Time-history of the maximum value of free-electron number density ($w_f = 7.3\,\mu$m, $f = 100$mm).

30 August 2023 12:22:34

Published under an exclusive license by AIP Publishing

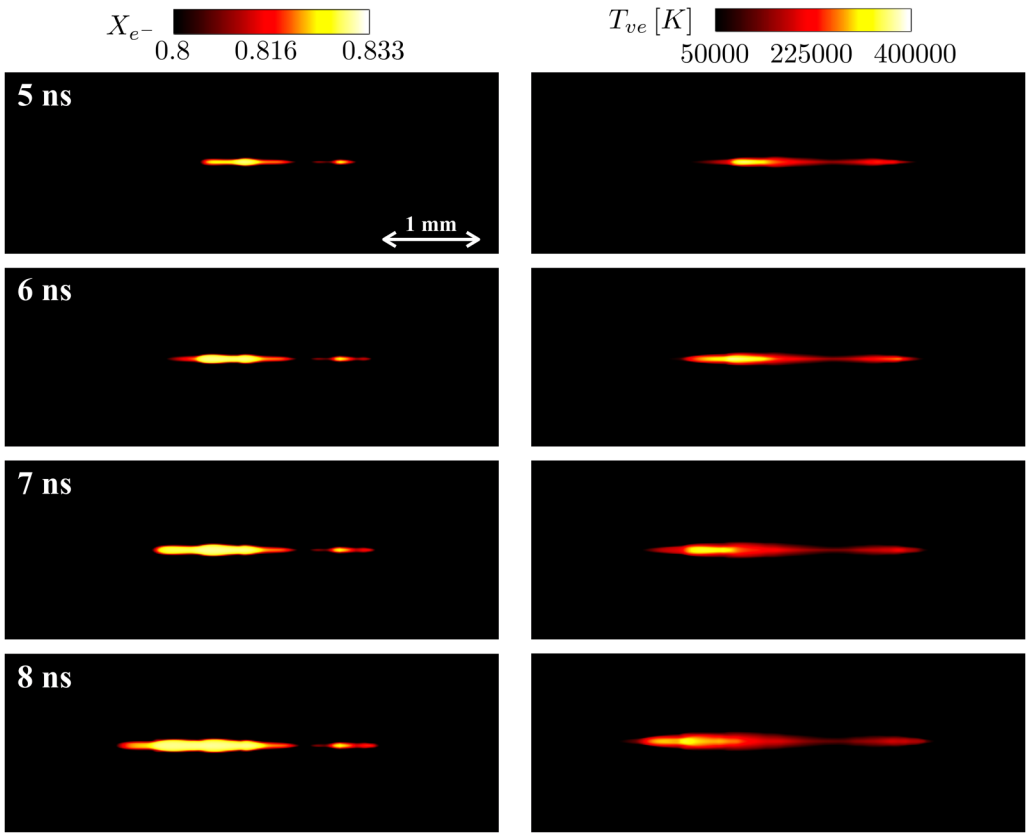

FIG. 6. Time-history of free-electron mole fraction (left) and temperature (right) for the 100mJ case ($w_f = 7.3\,\mu$m, $f = 100$mm).

30 August 2023 12:22:34

where the mode-beating function $g_{mb}(t) = [1 + A_{mb}\sin(2\pi f_{mb}t)]$, with A_{mb} and f_{mb} being, respectively, the corresponding non-dimensional amplitude and frequency, is introduced to modulate the Gaussian time dependence. The temporal standard deviation is obtained from $\sigma_t = \mathrm{FWHM}/2\sqrt{2\ln 2}$, where the Full-Width at Half Maximum (FWHM) is either taken from experiments or imposed. The radial standard deviation σ_r is determined based on the focal radius, beam diameter at focusing lens, and focal length,

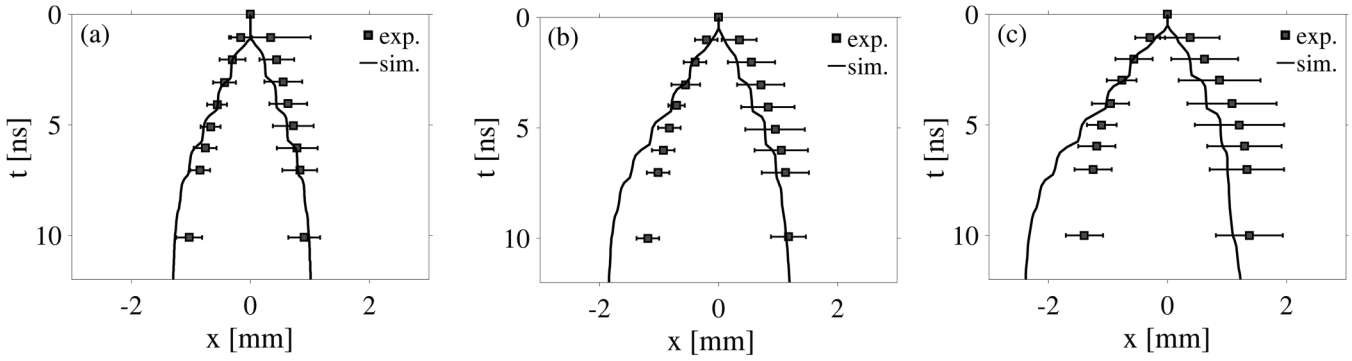

FIG. 7. x–t diagram comparing the predicted and the measured temporal evolution of the plasma boundaries along the optical axis at different energies: (a) 30mJ, (b) 60mJ, and (c) 100mJ ($w_f = 7.3\,\mu$m, $f = 100$mm). Time increases top-to-bottom. Focal point at $x = 0$mm.

Published under an exclusive license by AIP Publishing

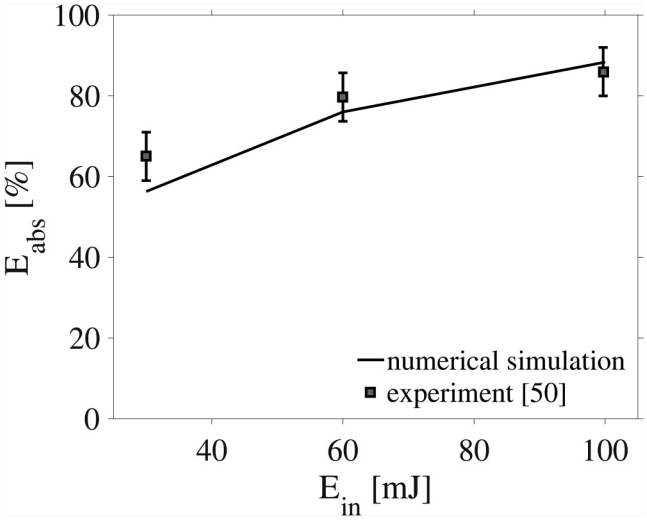

FIG. 8. Comparison between predicted and experimental absorbed energy ($w_f = 10\,\mu$m, $f = 80$mm).

assuming a diffraction limited par-axial beam. The procedure is discussed in Ref. 37. The duration of the pulse is taken as $t_p = 6\,\sigma_t$. The I_0 constant is determined by imposing that the energy entering the domain at $x = x_b$ is equal to that delivered by the laser (ε),

$$\varepsilon = 2\pi \int_0^{+\infty} \int_0^{t_p} I_\lambda(x_b, r, t)\, r\, dr\, dt = 2\pi\sigma_r^2 I_0 \int_0^{6\sigma_t} g_{mb}(t) \exp\left[-\frac{(t-3\sigma_t)^2}{2\sigma_t^2}\right] dt. \quad (7)$$

The flowfield is initialized in a quiescent and uniform state with ambient pressure and temperature equal to $p_a = 101325$Pa and $T_a = 288$K, respectively, to match the conditions of Ref. 50. In all simulations, the beam wavelength is $\lambda = 532$nm.

B. Model validation

The non-equilibrium LIB model developed by the authors has been extensively validated through comparison against experiments for single-mode pulses.[38,39] Here, the validation is pursued, further considering a multi-mode pulse. Experimental data are taken from the work by Nishihara *et al.*[50] who investigated LIB in atmospheric air at three different energies: 30, 60, and 100 mJ. For the sake of a more consistent comparison, the temporal part of the incoming intensity (6) is replaced here by a multi-mode waveform obtained by fitting the data from Nishihara *et al.* [i.e., from Fig. 3(b) of Ref. 50],

$$I_\lambda(x_b, r, t) = I_0 I_\lambda(x_b, r) I_\lambda(t) = I_0 \exp\left(-\frac{r^2}{2\sigma_r^2}\right) \max\left[\sum_{k=1}^{8} a_k \sin(b_k t + c_k), 0\right], \quad (8)$$

where the a_k, b_k, and c_k fit coefficients (for $0 \le t \le 18$ns) are given in Table I. The I_0 constant is always determined based on Eq. (7). Figure 3 compares the fitted multi-mode waveform [i.e., the bracketed term in Eq. (8)] with the experimental profile.

In all simulations conducted for validation purposes, the beam diameter at the focusing lens (with focal length $f = 100$mm) is 9.8 mm, whereas its focal radius is $w_f = 7.3\,\mu$m (as computed in Ref. 38). The value of the focal radius is within the prediction by Nishihara *et al.*,[50] who calculated a focal radius of $10\,\mu$m in the absence of fluid expansion using the razor edge method, and considered this result an over-estimate of the actual value.[50,63]

Figure 4 compares the computed absorbed energy with the measured non-transmitted energy. The agreement is good as the calculated absorbed energies fall within the experimental error bounds. At the end of the pulse ($t = 18$ns), the maximum electron number density is between 5.1×10^{19} and 9.6×10^{19} cm^{-3} (depending on the laser energy, see Fig. 5), consistently with what was reported in Ref. 50.

For a single-mode pulse, the plasma kernel forms at the point of maximum intensity (i.e., at the focal point). The *priming* electrons formed there to trigger the cascade ionization, and the plasma becomes opaque as a result of energy absorption via IB. The free-electron temperature increases faster than that of heavy-

30 August 2023 12:22:34

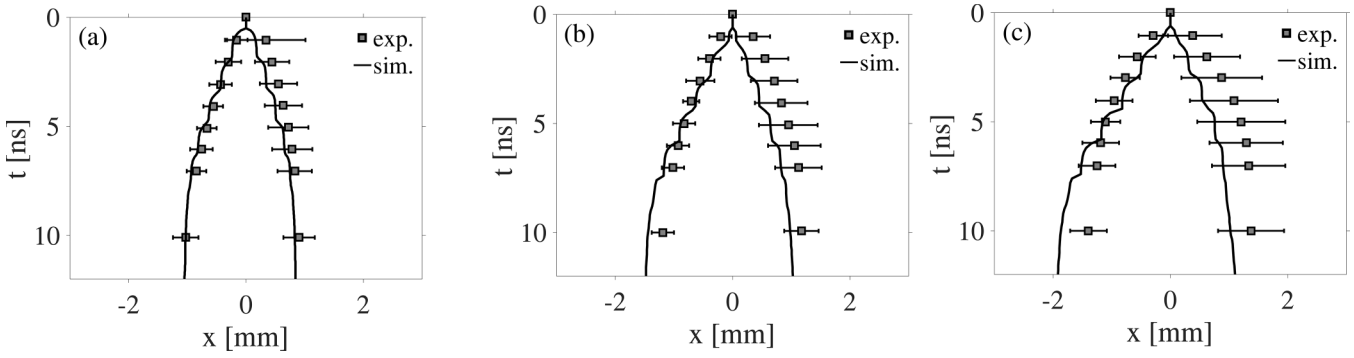

FIG. 9. *x*–*t* diagram comparing the predicted and the measured temporal evolution of the plasma boundaries along the optical axis at different energies: (a) 30mJ, (b) 60mJ, and (c) 100mJ ($w_f = 10\,\mu$m, $f = 80$mm). Convention for the axes is the same as of Fig. 7.

Published under an exclusive license by AIP Publishing

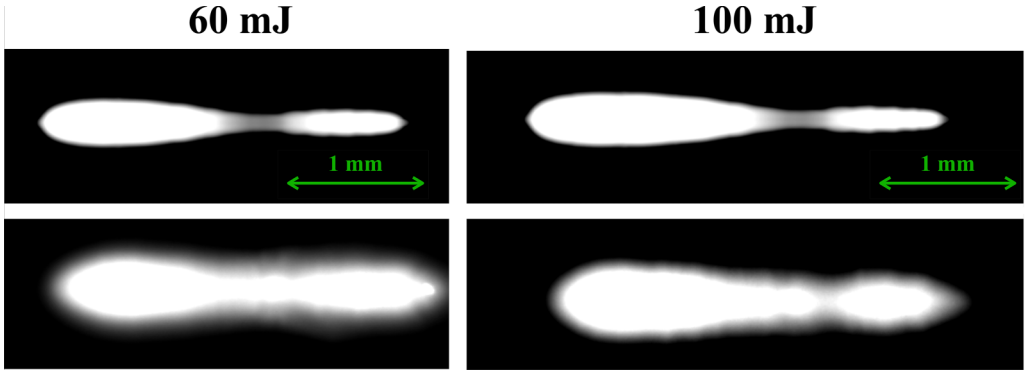

FIG. 10. Plasma emission images at the end of the pulse ($t = 18$ns): top simulations ($w_f = 10\,\mu$m, $f = 80$mm), bottom experiments.

particles (up to more than 10^5 K),[32,34,36,38] and a two lobe structure forms, with a rear lobe moving toward the laser source and a front lobe going in the opposite direction (*backward* and *forward* plasma waves, respectively).[38,64,65] It is worth recalling that the current model does not account for energy emission from the hot plasma kernel (that can be partly absorbed by the surrounding colder layer). Previous efforts from the authors[38,47] have shown that the inclusion of energy emission and re-absorption by means of a diffusion approximation for radiative transfer is associated with a decrease of temperature and a radially larger plasma kernel. We omit these effects here for simplicity. After the laser-source is turned off, the plasma propagates within the cold surrounding gas, and in the first hundreds of nano-seconds the free-electron and heavy-particle temperatures equilibrate with each other and decrease down to $10\,000 - 50\,000$ K.[39,40,66–70] With multi-mode beating, the breakdown dynamics is similar. However, as put in evidence by experiments,[50] the growth of the plasma kernel is accompanied by the development of local inhomogeneities. These are also observed in the current simulations as shown by the time-history of the mole fraction of free-electrons and their temperature in Fig. 6, and by the evolution of the maximum value of the free-electron number density reported in Fig. 5. A comparison with the laser time-history (see Fig. 3) indicates that the above local maxima are attained at the peaks of the laser power, suggesting the existence of a direct relation between the mode-beating frequency and the observed quasi-periodic structures. These matters are investigated in more detail in Sec. III C. Figure 7 reports the evolution of the plasma boundaries along the optical axis. For the simulations, the nominal plasma edge is taken to be the peak of the gradient of the mole fraction of free-electrons. Overall, the predicted evolution is in good agreement with the experiments (3σ bounds are shown for the observations). The observed differences are thought to be primarily associated with the variability in the breakdown location, which Nishihara *et al.*[50] quantify for the multi-mode cases to be of the order of 0.4 mm. In addition, some parameters cannot be easily measured presently, which add a systematic uncertainty. In order to assess the effect of these uncertainties on the simulations, further calculations were conducted by changing the focal length

30 August 2023 12:22:34

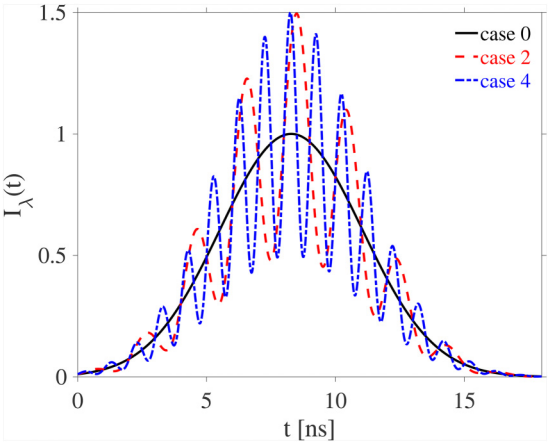

FIG. 11. Temporal beam waveforms for cases 0 (Gaussian), 2, and 4.

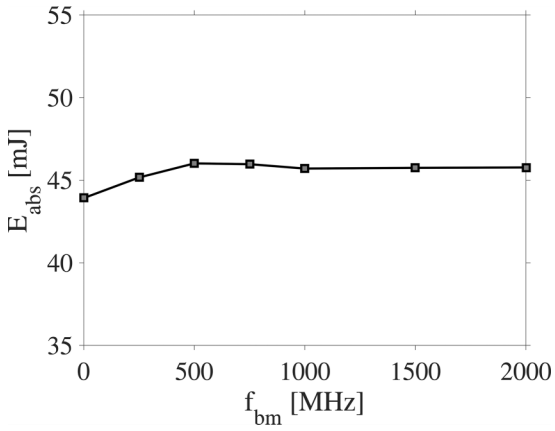

FIG. 12. Absorbed energy for cases 0 (Gaussian) through 6.

Published under an exclusive license by AIP Publishing

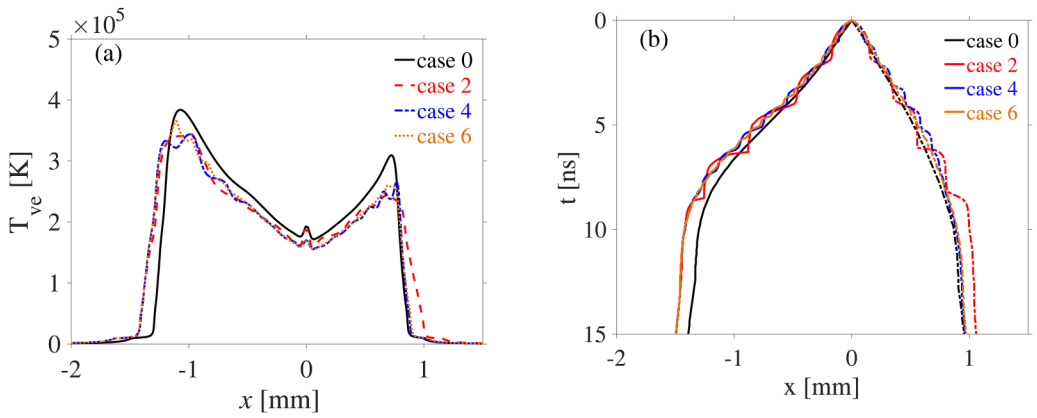

FIG. 13. (a) Free-electron temperature along the optical axis for cases 0 (Gaussian), 2, 4, and 6 at $t = 10$ns and (b) x–t diagram of plasma boundary evolution along the optical axis (solid lines are rear lobe and broken lines are front lobe).

up to 20 % of the nominal value of 100 mm, and by setting the focal radius equal to the upper-bound of 10 μm determined by Nishihara *et al.* via the razor edge method.[50] The results in terms of absorbed energy and evolution of the plasma boundaries along the optical axis are reported in Figs. 8 and 9, respectively. With the modified beam and optics parameters, the calculated plasma boundary evolution is in better agreement with the experiments. In analogy with the results of Fig. 7, where nominal values are used, the agreement worsens with increasing energy. A similar trend is also observed when comparing the emission images as done in Fig. 10 (details on the procedure to construct emission images from simulations may be found in Ref. 38).

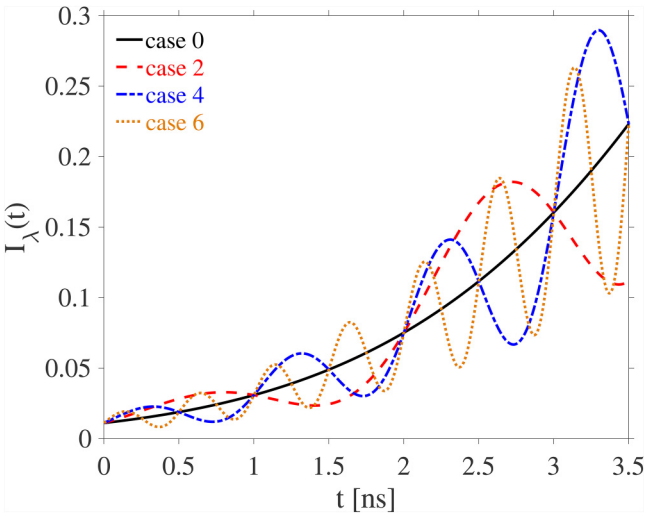

FIG. 14. Temporal beam waveform for cases 0 (Gaussian), 2, 4, and 6 in the time interval $0 \leq t \leq 3.5$ns.

C. Plasma formation mechanism: Effect of mode-beating

The discussion in Sec. III B has shown that the LIB model is able to reproduce the two-lobed structure and its quasi-periodic spots observed in experiments for multi-mode pulses.[50] Here, the effect of the mode-beating on plasma formation is investigated in detail.

In all simulations, the incoming intensity distribution is evaluated based on Eq. (6) (no experimental data used) for the purpose of studying the effect of the mode-beating frequency on the breakdown dynamics. A total of seven cases (0–6) is here considered. Case 0 is a purely Gaussian pulse (i.e., $A_{mb} = 0$), whereas cases 1 through 6 represent multi-mode pulses with non-dimensional amplitude $A_{mb} = 0.5$, and mode-beating frequencies f_{mb} equal to 250, 500, 750, 1000, 1500, and 2000 MHz. For all cases, the temporal FWHM, the laser energy, and the focal length are 6.5 ns, 60 mJ, and 75 mm, respectively. All the other parameters (e.g., ambient conditions, focal radius) are the same as the baseline values of Sec. III B. The temporal beam waveforms for cases 0 (Gaussian), 2, and 4 are plotted in Fig. 11.

Figure 12 displays the absorbed energy for cases 0 through 6. The plotted data show an increase of the absorbed energy up to frequencies $\approx$ 500MHz. For larger values, the absorbed energy undergoes a small decrease before approaching a flat profile. Energy deposition is maximum for case 2, though the increase with respect to the single-mode (i.e., Gaussian) case is modest (≈2%–3%). The above results may be explained based on the fact that, during the time intervals when the mode-beating function is $g_{mb}(t) > 1$, the intensity is larger than that of the corresponding Gaussian pulse (see also Fig. 11). Since the volumetric rate of energy deposition via IB is proportional to the intensity (i.e., $\Omega = \kappa I$), this leads to larger absorbed energies. The effect becomes more and more negligible beyond a threshold frequency since higher frequencies shorten the time interval during which $g_{mb}(t) > 1$. Changing the mode-beating frequency affects also the growth of the plasma kernel, as demonstrated by the free-electron temperature profiles

30 August 2023 12:22:34

Published under an exclusive license by AIP Publishing

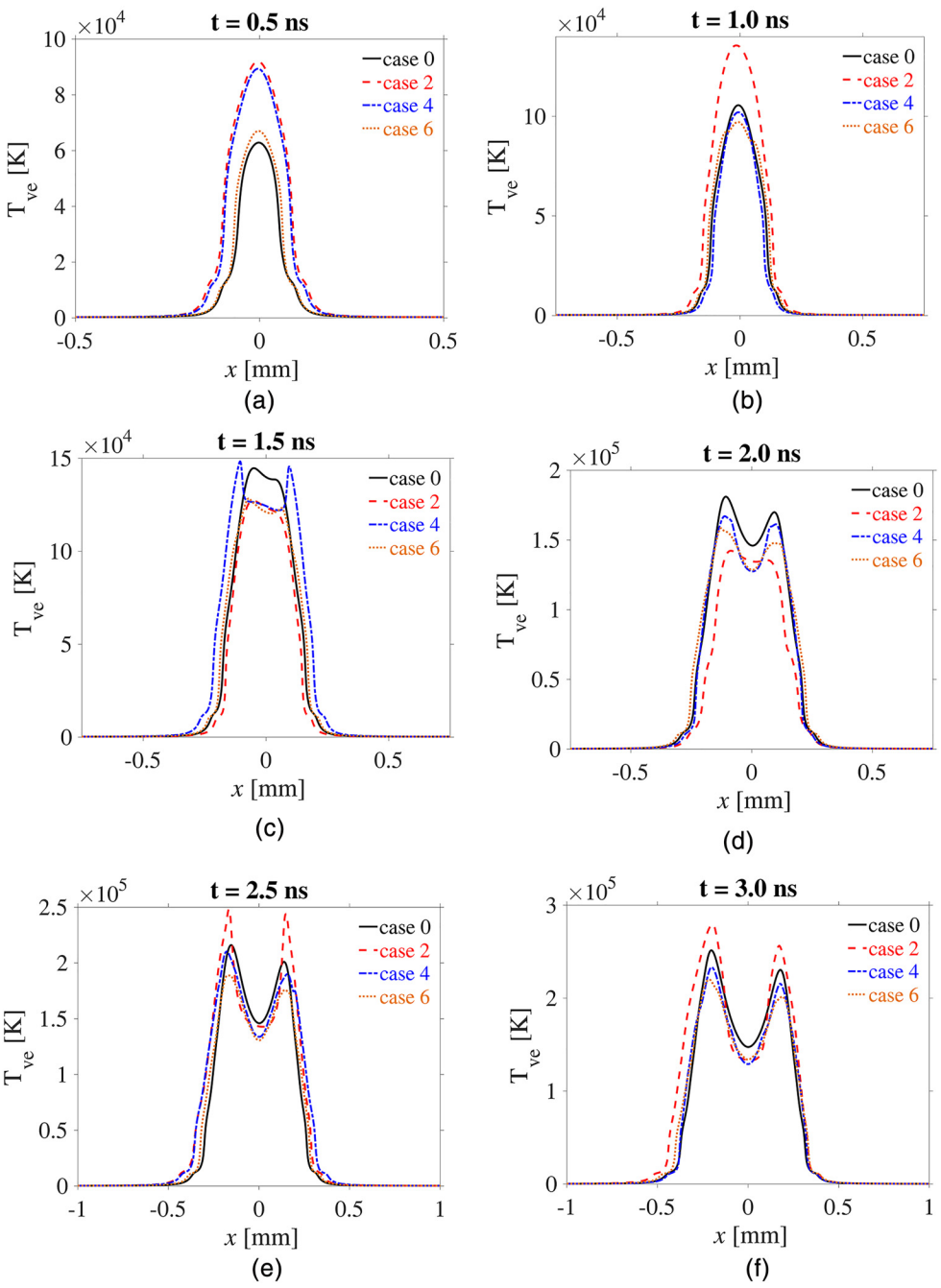

FIG. 15. Temporal evolution of the free-electron temperature along the optical axis for cases 0 (Gaussian), 2, 4, and 6 in the time interval $0 \leq t \leq 3.5$ns.

and x–t diagrams in Fig. 13. In general, the multi-mode pulses lead to a more elongated plasma compared to the single-mode case. This finding is consistent with the above discussion on absorbed energy. Among the multi-mode results, case 2 leads to a larger front lobe than cases 4 and 6, whereas the differences are barely noticeable for the rear lobe. This is a consequence of the fact that, at the rear lobe, energy deposition is essentially dependent only on the instantaneous value of the intensity,

30 August 2023 12:22:34

Published under an exclusive license by AIP Publishing

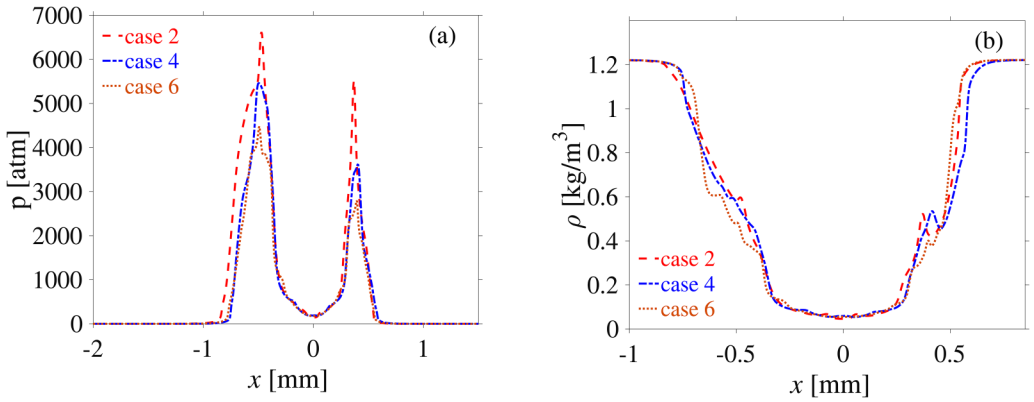

FIG. 16. Distribution of pressure (a) and density (b) along the optical axis at $t = 5$ns.

which is the reason why, toward the end of the pulse, all multi-mode plasma boundary profiles collapse onto the same curve. On the other hand, energy deposition at the front lobe is affected by beam attenuation which, in turn, depends not only on the instantaneous optical properties (e.g., absorption coefficient) but also on the time-history of the pulse since the latter has an influence on the evolution of the plasma kernel.

The impact of the beam temporal waveform on the plasma dynamics may be observed when monitoring the free-electron temperature. This is done in Fig. 15 showing the evolution of the latter quantity along the optical axis at the onset of breakdown (i.e., $0 \leq t \leq 3.5$ns). For the sake of convenience, the beam waveform for the considered time-frame is also reported in Fig. 14. During $0 \leq t \leq 1$ns, the intensity is larger for case 2 and the associated free-electron temperature rises faster than cases 4 and 6, as shown by the frames extracted at $t = 0.5$ns and $t = 1.0$ns. The same behavior is observed for cases 4 and 6 during the intervals $1 \leq t \leq 1.5$ns and $1.5 \leq t \leq 2.0$ns, respectively, which correspond to the regions where the related mode-beating functions attain local maxima. Proceeding further in time, another power-peak phase for case 2 is entered, leading to a new sharp rise of the free-electron temperature around $t = 2.5$ns. Overall, the amplitude-modulation of a baseline Gaussian pulse alters the heating rate of the plasma, compared to the single-mode case, as revealed by the observed sudden rises of the free-electron temperature.

At $t \approx 5$ns, the large increase of pressure associated with the absorbed laser energy [see Fig. 16(a)] generates a strong gas-dynamic expansion in the plasma core, as can be observed from the density distribution reported in Fig. 16(b). The sudden expansion generates a reduction of the gas density and, consequently, a decrease of the absorption coefficient. This, together with the low power portion of the laser temporal history for case 2 during the interval $5 \leq t \leq 6$ns (see Fig. 17), prevents the free-electron temperature from rising again (i.e., the sudden expansion compensates for the IB energy absorption), as it can be observed in Fig. 18 (top right for 5 and 6ns). In turn, a larger fraction of the laser radiation is able to escape the plasma rear lobe and be absorbed by the front lobe. The same does not occur for cases 4 and 6 since, in the same time interval, at least one new peak of the laser intensity temporal history deposits enough energy to sustain the growth of the rear lobe as shown in Fig. 18, with the consequence that radiation attenuation precludes the laser energy from being efficiently deposited in the front lobe at later times. The overall effect on plasma formation is shown in Fig. 19, which compares the evolution of the mole fraction of free-electrons of cases 2 and 4. Increasing the mode-beating frequency leads to a more homogeneous plasma resembling the tear-drop morphology of a single-mode pulse.[38]

Figure 20 shows the temporal evolution of the velocity magnitude at 8, 12, and 16ns for cases 0 (Gaussian), 2, 4, and 6. Mode-beating results in more irregular velocity profiles; however, no overall amplification is observed compared to case 0 (i.e., Gaussian pulse). The velocity contours are analogous for all cases,

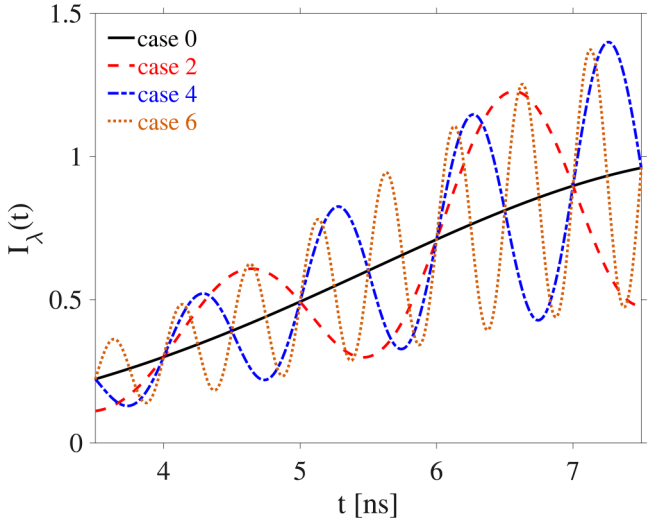

FIG. 17. Temporal beam waveform for cases 0 (Gaussian), 2, 4, and 6 in the time interval $3.5 \leq t \leq 7.5$ns.

30 August 2023 12:22:34

Published under an exclusive license by AIP Publishing

suggesting that for the conditions investigated in this work hydrodynamic instability is not responsible for the onset of the plasma kernels since there is no evidence of amplifying instabilities associated with the inflectional velocity profiles.

In order to assess the cause of the observed local inhomogeneities (i.e., quasi-periodic structures) in the plasma kernel, the evolution of the maximum values of the number density of free-electrons and the plasma boundary (using the x–t diagram) are monitored for cases 1 through 6 (see Fig. 21). It may be seen that the alternation between local maxima and minima, in the maximum number density plots, occurs with a period of $\approx$ 2ns for case 2, $\approx$ 1ns for case 4, and $\approx$ 0.5ns for case 6. Those values

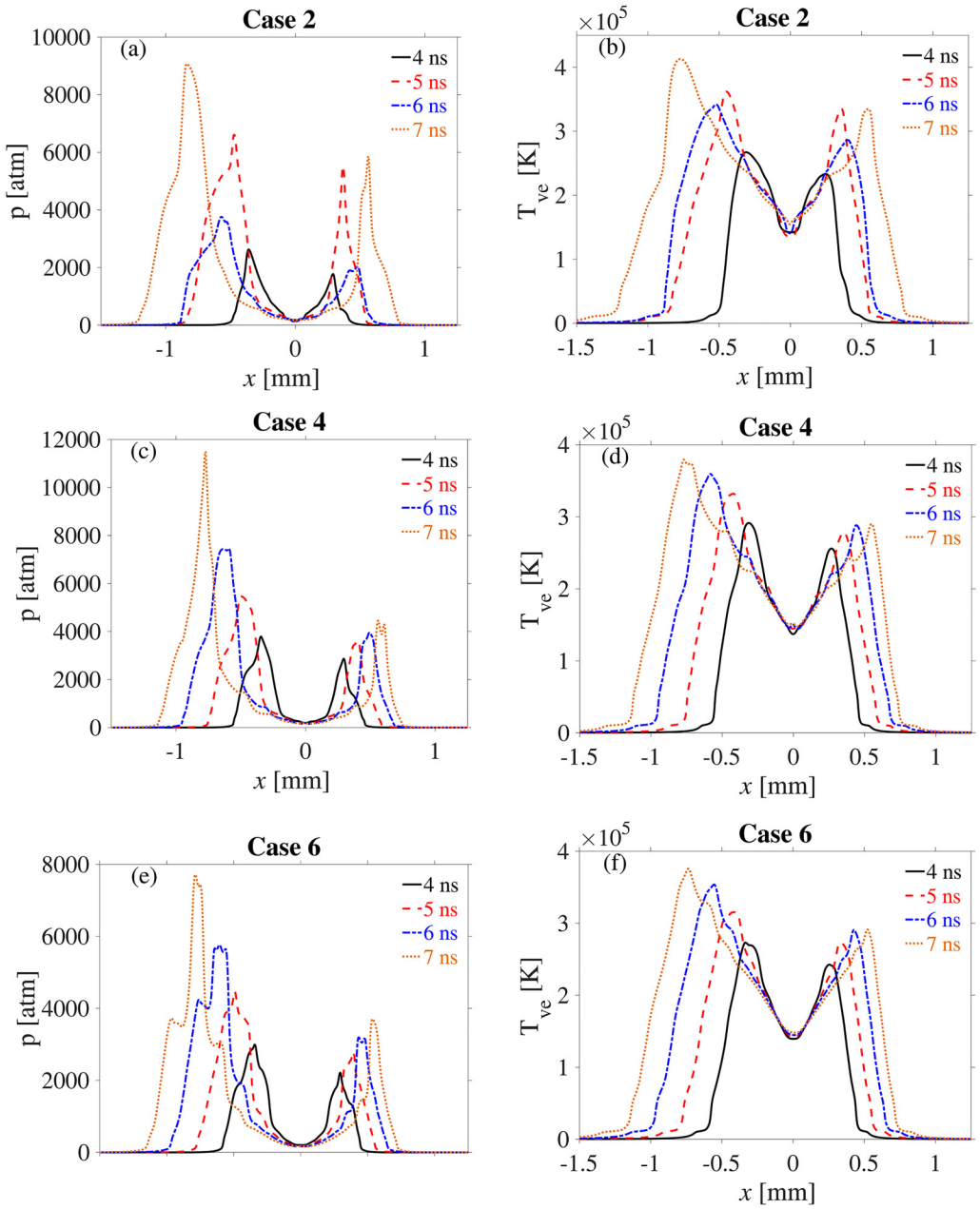

FIG. 18. Temporal evolution of the distribution of pressure [(a), (c), and (e)] and free-electron temperature [(b), (d), and (f)] along the optical axis.

30 August 2023 12:22:34

Published under an exclusive license by AIP Publishing

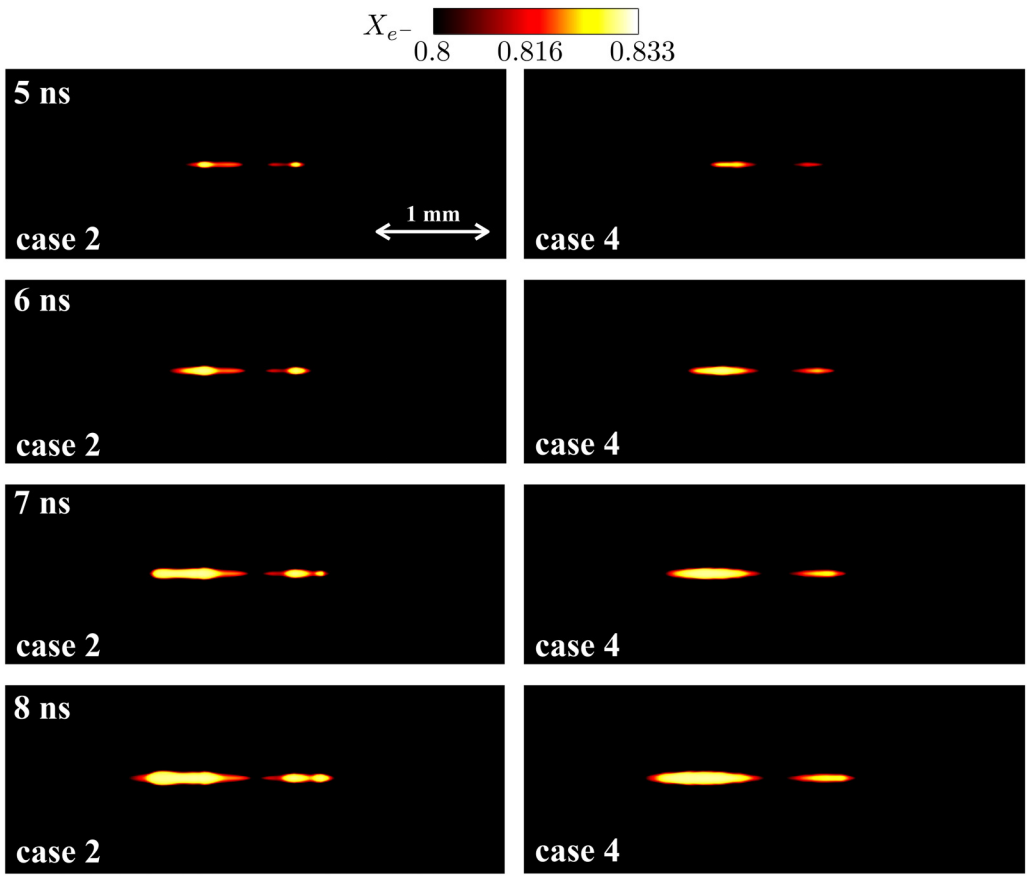

FIG. 19. Temporal evolution of the mole fraction of free-electrons for cases 2 and 4 highlighting local inhomogeneities resulting from the multi-mode operating fashion.

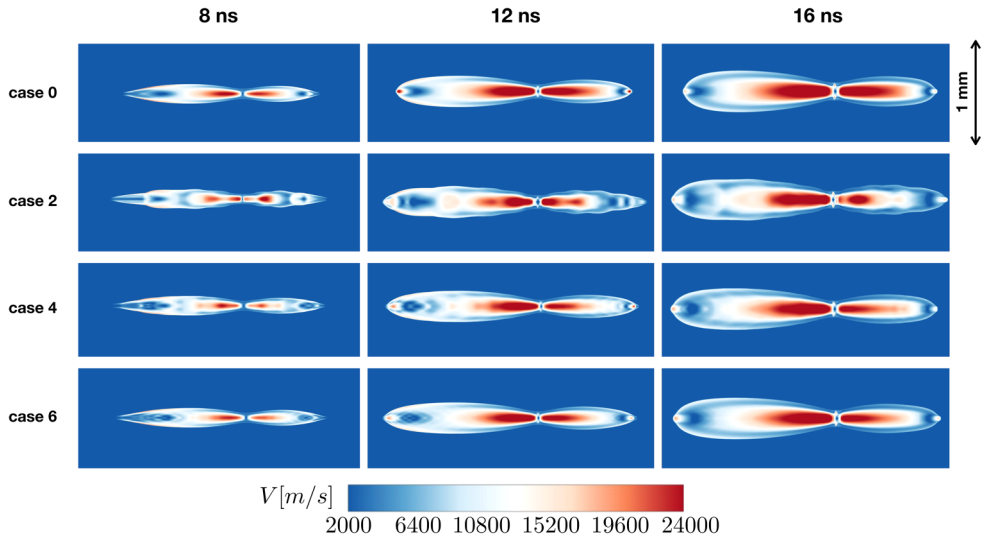

FIG. 20. Temporal evolution of the velocity field during the laser discharge.

30 August 2023 12:22:34

Published under an exclusive license by AIP Publishing

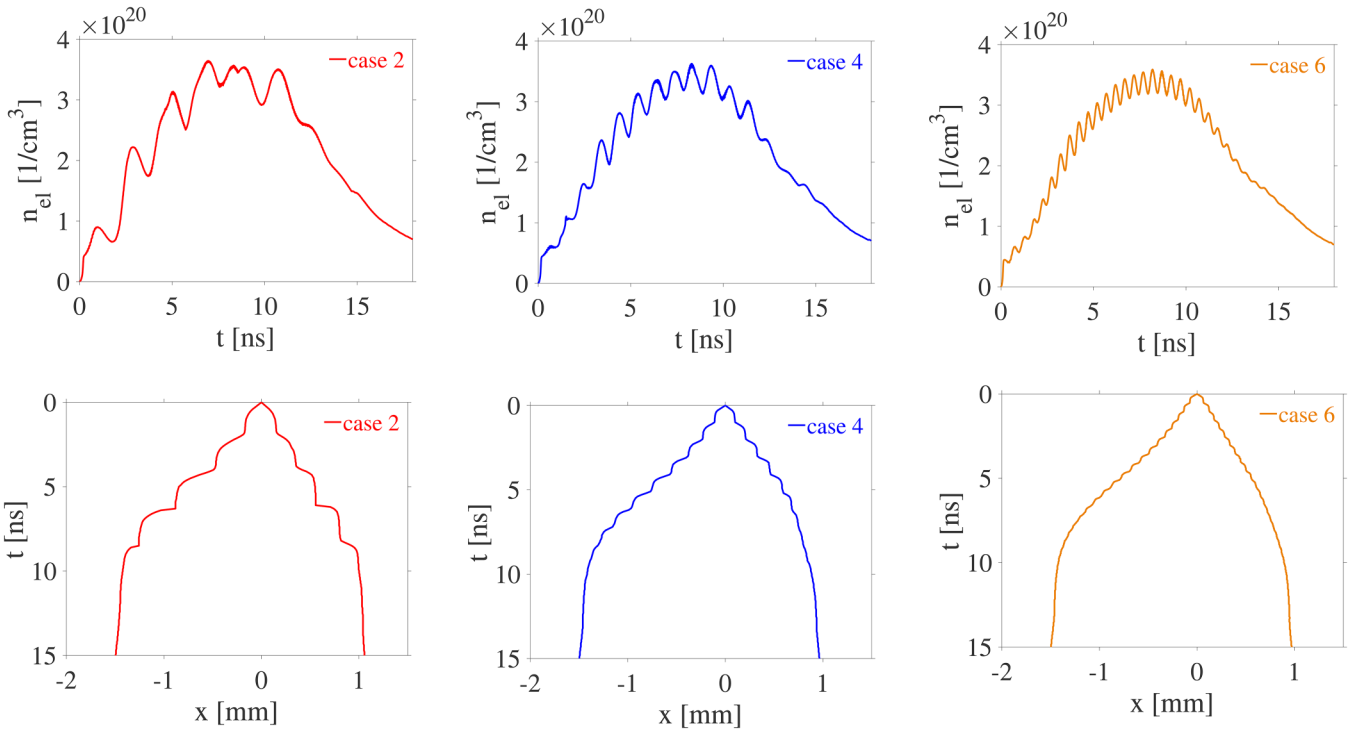

FIG. 21. Temporal evolution of the maximum number density of free-electrons (top) and *x*–*t* diagram of plasma boundary along the optical axis (bottom).

30 August 2023 12:22:34

are precisely the inverse of the mode-beating frequencies (i.e., periods) of the corresponding cases: $1/500\text{MHz}^{-1}$ for case 2, $1/1000\text{MHz}^{-1}$ for case 4, and $1/2000\text{MHz}^{-1}$ for case 6. To put these observations on a quantitative basis, the predicted maximum number density data for case 4 are compared with an amplitude-modulated Gaussian fit, which mimics the time dependence of the laser beam (see Fig. 22),

$$n_e^{\max} = n_0[a_1 + a_2 \sin(2\pi a_3 t + a_4)] \exp\left[-\frac{(t - a_5/2)^2}{2a_6^2}\right], \quad (9)$$

where $n_0 = 5.5e + 20\text{cm}^{-3}$, $a_1 = 0.6219$, $a_2 = 0.04116$, $a_3 = 992.2\text{MHz}$, $a_4 = -0.4493$, $a_5 = 16.27\text{ns}$, and $a_6 = 4.829\text{ns}$. The results of the simulation are in very good agreement with Eq. (9). Moreover, the value of the a_3 coefficient, which represents the modulation frequency of the signal (9), is very close to the mode-beating frequency of case 4 (i.e., 1 000 MHz). Similar outcomes are found for the other multi-mode cases investigated here. The results in Fig. 22 seem to suggest that the observed quasi-periodic structures are directly linked to the mode-beating frequency and not induced by hydrodynamic instabilities. In a similar fashion of single-mode lasers,[38] the spatiotemporal evolution of the plasma and the formation of the kernels is triggered by multiphoton ionization, which creates priming electrons in the undisturbed gas at the edges of the evolving plasma. Then, the mechanism is sustained by energy deposition via inverse Bremsstrahlung, which counteracts the energy losses due to the cascade ionization. The dynamics of the plasma lobes is guided by both multiphoton ionization and ionization by electron impact, with a strong radial plasma expansion that prevents the

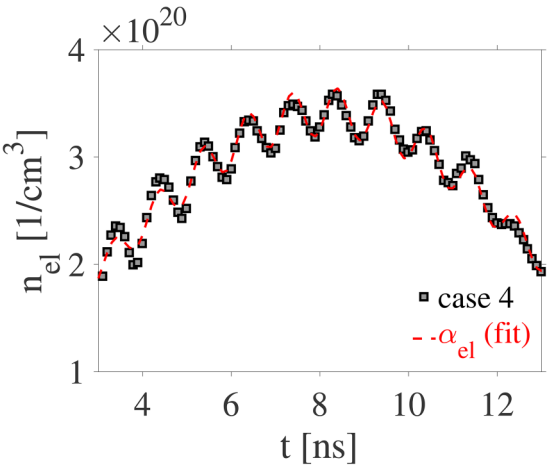

FIG. 22. Maximum value of the number density of free-electrons during the multi-mode discharge for case 4 (symbol) compared with amplitude-modulated Gaussian fit (9) (broken line).

Published under an exclusive license by AIP Publishing

plasma kernel from becoming completely opaque to the incoming radiation.

IV. CONCLUSIONS

This work discussed the application of a physical model, previously developed by the authors, to study the effects of mode-beating on the dynamics of laser-induced gaseous plasmas. The plasma was treated via a fluid approach based on the Navier–Stokes equations. Non-equilibrium effects were accounted for based on a two-temperature model. The propagation and attenuation of the laser beam were modeled by means of the radiative transfer equation, which was self-consistently coupled to the flow governing equations. Numerical solutions were obtained based on an Implicit-Explicit (IMEX) finite volume method.

Applications considered laser-induced breakdown in atmospheric air for nano-second multi-mode pulses, constructed based on amplitude-modulated Gaussian time-profiles. The results of the simulations were first compared with experiments for the sake of validation. An overall good agreement was observed for the absorbed energy, evolution of the plasma boundary, and electron number density at the end of the discharge. The calculations were also able to reproduce key features found in experiments: a two-lobed plasma kernel (as in the single-mode configuration) and the formation of quasi-periodic structures. It is worth mentioning that this was achieved without seeding the ambient gas with an artificial plasma (as often done in the literature). An analysis of the results showed that the quasi-periodic structures are strongly affected by the mode-beating frequency, as observed also experimentally, and that their occurrence corresponds to the local power peaks of the incident beam. Moreover, the simulations suggest that the laser mode-beating frequency does not appear to seed hydrodynamic instabilities (via interaction between excited and transmitted waves at the plasma surface) but instead directly leads to the periodic kernel structures that correspond to the operating beating mode. The modulation frequency of the laser determines the local electron density and temperature, with the multi-mode pulses leading to a more elongated plasma, compared to the single-mode case. This depends on the correlation between the temporal peaks/valleys of the laser pulse and the gas-dynamic expansion of the plasma core that influences the heating rate with the laser radiation being able (or not) to escape more effectively the plasma rear lobe and being absorbed by the front lobe. Future work will focus on characterizing the breakdown mechanism dependence on multi-mode change of phase of laser intensity due to constructive or destructive interference between modes.

ACKNOWLEDGMENTS

This material was based in part upon the work supported by the Department of Energy, National Nuclear Security Administration under Award No. DE-NA0002374. The authors gratefully acknowledge Dr. J. H. Cooley and Dr. T. Wada for the useful scientific discussions.

AUTHOR DECLARATIONS

Conflict of Interest

The authors declare no potential conflicts of interest with respect to the research, authorship, and publication of this article.

DATA AVAILABILITY

The data that support the findings of this study are available within the article.

APPENDIX: THE EQUATION OF RADIATIVE TRANSFER

In this work, the radiation field is modeled with a kinetic approach through the Radiative Transfer Equation (RTE). The labeling kinetic approach stems from kinetic theory and means that radiation is treated as a photon gas described by the one-particle distribution function $f = f(\mathbf{r}, \mathbf{p}, t)$, where $\mathbf{r}$ and $\mathbf{p}$ denote position and momentum, respectively, whereas t is time. The monochromatic intensity $I_\lambda = I_\lambda(\mathbf{r}, \Omega, t)$ is related to the distribution function by[41]

$$I_\lambda = \frac{c^2 h_P^4}{\lambda^5} f, \tag{A1}$$

where c is the vacuum speed of light and h_P is Planck's constant. The RTE is obtained via the combined use of Eq. (A1) and the kinetic equation for f (see Ref. 41 for more details). As the above assumptions imply, the RTE may account for emission, absorption, and scattering of light within the boundaries of geometric optics. The effects of refraction and polarization may also be included at the price of a more complicated formulation.

In alternative to the RTE, one may consider Maxwell's equations. Here, dispersive and dissipative effects are contained in the constitutive relations. For instance, the electric displacement (in the frequency domain) for isotropic media may be written as

$$\mathbf{D}(\omega) = \varepsilon(\omega)\mathbf{E}(\omega), \tag{A2}$$

where $\varepsilon = \varepsilon(\omega)$ is the medium (complex) dielectric function in the frequency domain. In the time domain, Eq. (A2) translates into a convolution integral. The main advantage of Maxwell's equations compared to an RTE-based approach is the possibility of including wave phenomena (e.g., diffraction) that cannot be described by geometric optics.

REFERENCES

[1]L. J. Radziemski and D. A. Cremers, *Laser-Induced Plasmas and Applications* (CRC Press, 1989).
[2]C. G. Morgan, "Laser-induced breakdown of gases," Rep. Prog. Phys. **38**, 621 (1975).
[3]G. V. Ostrovskaya *et al.*, "Laser spark in gases," Sov. Phys. Usp. **16**, 834 (1974).
[4]C. G. Morgan, "Laser-induced breakdown phenomena," Sci. Prog. **65**, 31–50 (1978). https://www.jstor.org/stable/43420443
[5]Y. P. Raizer, "Optical discharges," Sov. Phys. Usp. **23**, 789–806 (1980).
[6]L. Massa, J. Retter, N. G. Glumac, G. S. Elliot, and J. B. Freund, "Fluid-plasma coupling in hydrogen flames," in *APS Division of Fluid Dynamics Meeting Abstracts* (American Physical Society, 2015).
[7]L. Massa and J. B. Freund, "Plasma-combustion coupling in a dielectric-barrier discharge actuated fuel jet," Combust. Flame **184**, 208–232 (2017).

30 August 2023 12:22:34

Published under an exclusive license by AIP Publishing

[8]S. M. Starikovskaia, "Plasma assisted ignition and combustion," J. Phys. D: Appl. Phys. **39**, R265 (2006).
[9]R. Mahamud, A. A. Tropina, M. N. Shneider, and R. B. Miles, "Dual-pulse laser ignition model," Phys. Fluids **30**, 106104 (2018).
[10]C. Dumitrache and A. P. Yalin, "Numerical modeling of the hydrodynamics induced by dual-pulse plasma," in *2018 AIAA Aerospace Sciences Meeting* (AIAA, 2018), p. 0689.
[11]C. Dumitrache, C. Limbach, and A. P. Yalin, "Laser thermal ignition using a dual-pulse approach," in *54th AIAA Aerospace Sciences Meeting* (AIAA, 2016), p. 0460.
[12]C. Butte, C. Dumitrache, and A. P. Yalin, "Properties of dual-pulse laser plasmas and ignition characteristics in propane-air and methane-air mixtures," in *AIAA Scitech 2019 Forum* (AIAA, 2019), p. 0464.
[13]C. Dumitrache, R. VanOsdol, C. Limbach, and A. P. Yalin, "Control of early flame kernel growth by multi-wavelength laser pulses for enhanced ignition," Sci. Rep. **7**, 10239 (2017).
[14]T. Sato, A. Alberti, A. Munafò, M. Panesi, K. Matsuoka, A. Kawasaki, and J. Kasahara, "Numerical study on early-times laser controlled detonative propulsion," in *AIAA Scitech 2021 Forum* (AIAA, 2021), p. 0802.
[15]C. M. Limbach, "Characterization of nanosecond, femtosecond and dual pulse laser energy deposition in air for flow control and diagnostic applications," Ph.D. thesis (Princeton University, Princeton, 2015).
[16]D. D. Knight, "Survey of aerodynamic drag reduction at high speed by energy deposition," J. Propul. Power **24**, 1153–1167 (2008).
[17]N. Kianvashrad and D. D. Knight, "Non-equilibrium effects of interaction of laser discharge with hemisphere-cylinder in supersonic flow," in *2018 Flow Control Conference* (AIAA, 2018), p. 3757.
[18]A. Pournadali Khamseh and E. P. DeMauro, "Towards trajectory control of a supersonic projectile using laser energy deposition," in *AIAA Scitech 2019 Forum* (AIAA, 2019), p. 1347.
[19]A. Starikovskiy, C. Limbach, and R. B. Miles, "Trajectory control of small rotating projectiles by laser sparks," in *54th AIAA Aerospace Sciences Meeting* (American Institute of Aeronautics and Astronautics, 2016), p. 0459.
[20]N. Kianvashrad and D. D. Knight, "Nonequilibrium effects on prediction of aerothermodynamic loading for a double cone," AIAA J. **20**, 1–18 (2019).
[21]C. Trefny and V. Dippold, "Supersonic free-jet combustion in a ramjet burner," in *46th AIAA/ASME/SAE/ASEE Joint Propulsion Conference & Exhibit* (AIAA, 2010), p. 6643.
[22]C. J. Trefny, V. F. Dippold III, and S. Yungster, "Dual-mode free-jet combustor," NASA Technical Report (2017).
[23]A. Zheltovodov, E. Pimonov, and D. Knight, "Energy deposition influence on supersonic flow over axisymmetric bodies," in *45th AIAA Aerospace Sciences Meeting and Exhibit* (AIAA, 2007), p. 1230.
[24]R. G. Adelgren, H. Yan, G. S. Elliott, D. D. Knight, T. J. Beutner, and A. A. Zheltovodov, "Control of edney IV interaction by pulsed laser energy deposition," AIAA J. **43**, 256–269 (2005).
[25]A. Alberti, A. Munafò, C. Pantano, and M. Panesi, "Supersonic and hypersonic non-equilibrium flow control using laser energy deposition," in *AIAA Aviation 2019 Forum* (AIAA, 2019), p. 2867.
[26]A. Alberti, A. Munafò, C. Pantano, and M. Panesi, "Self-consistent computational fluid dynamics of supersonic drag reduction via upstream-focused laser-energy deposition," AIAA J. **59**, 1214–1224 (2021).
[27]A. P. Khamseh, R. M. Kiriakos, and E. P. DeMauro, "Stereoscopic particle image velocimetry of laser energy deposition on a Mach 3.4 flow field," Exp. Fluids **62**, 1–19 (2021).
[28]A. N. Panchenko, M. A. Shulepov, A. E. Tel'Minov, L. A. Zakharov, A. A. Paletsky, and N. M. Bulgakova, "Pulsed IR laser ablation of organic polymers in air: Shielding effects and plasma pipe formation," J. Phys. D: Appl. Phys. **44**, 385201 (2011).
[29]G. Colonna, A. Casavola, and M. Capitelli, "Modelling of LIBS plasma expansion," Spectrochim. Acta, Part B **56**, 567–586 (2001).
[30]S. Musazzi and U. Perini, "LIBS instrumental techniques," in *Laser-Induced Breakdown Spectroscopy* (Springer, 2014), pp. 59–89.
[31]S. S. Harilal, P. J. Skrodzki, A. Miloshevsky, B. E. Brumfield, M. C. Phillips, and G. Miloshevsky, "On-and off-axis spectral emission features from laser-produced gas breakdown plasmas," Phys. Plasmas **24**, 063304 (2017).
[32]C. De Michelis, "Laser induced gas breakdown: A bibliographical review," IEEE J. Quantum Electron. **5**, 188–202 (1969).
[33]Y. B. Zel'dovich and Y. P. Raizer, "Cascade ionization of a gas by a light pulse," Sov. Phys. JETP **20**, 772 (1965).
[34]Y. B. Zel'dovich and Y. P. Raizer, *Physics of Shock Waves and High-Temperature Hydrodynamic Phenomena* (Academic Press Inc., New York, 1967).
[35]D. Bradley, C. G. W. Sheppard, I. M. Suardjaja, and R. Woolley, "Fundamentals of high-energy spark ignition with lasers," Comb. Flame **138**, 55–77 (2004).
[36]T. X. Phuoc and F. P. White, "An optical and spectroscopic study of laser-induced sparks to determine available ignition energy," Proc. Combust. Inst. **29**, 1621–1628 (2002).
[37]A. Munafò, A. Alberti, C. Pantano, J. B. Freund, and M. Panesi, "A computational model for nanosecond pulse laser-plasma interactions," J. Comp. Phys. **406**, 109190 (2020).
[38]A. Alberti, A. Munafò, M. Koll, M. Nishihara, C. Pantano, J. B. Freund, G. Elliott, and M. Panesi, "Laser-induced non-equilibrium plasma kernel dynamics," J. Phys. D: Appl. Phys. **53**(2), 025201 (2019).
[39]A. Alberti, A. Munafò, C. Pantano, J. B. Freund, and M. Panesi, "Collinear dual-pulse laser optical breakdown and energy deposition," J. Phys. D: Appl. Phys. **53**, 205202 (2020).
[40]S. S. Harilal, B. E. Brumfield, and M. C. Phillips, "Lifecycle of laser-produced air sparks," Phys. Plasmas **22**, 063301 (2015).
[41]J. Oxenius, *Kinetic Theory of Particles and Photons: Theoretical Foundations of Non-LTE Plasma Spectroscopy* (Springer Science & Business Media, 2012), Vol. 20.
[42]R. Kandala and G. V. Candler, "Numerical studies of laser-induced energy deposition for supersonic flow control," AIAA J. **42**, 2266–2275 (2004).
[43]A. A. Tropina, R. B. Miles, and M. N. Shneider, "Mathematical model of dual-pulse laser ignition," J. Prop. Power **34**, 408–414 (2017).
[44]S. Sai Shiva, C. Leela, P. Prem Kiran, C. D. Sijoy, V. R. Ikkurthi, and S. Chaturvedi, "Numerical investigation of nanosecond laser induced plasma and shock wave dynamics from air using 2D hydrodynamic code," Phys. Plasmas **24**, 083110 (2017).
[45]R. Mahamud, A. A. Tropina, M. N. Shneider, and R. B. Miles, "Dual-pulse laser ignition model," Phys. Fluids **30**, 106104 (2018).
[46]A. Casavola, G. Colonna, A. De Giacomo, O. De Pascale, and M. Capitelli, "Experimental and theoretical investigation of laser-induced plasma of a titanium target," Appl. Opt. **42**, 5963–5970 (2003).
[47]A. Alberti, "Multi-scale modeling of laser induced breakdown in non-equilibrium plasmas," Ph.D. thesis (University of Illinois at Urbana-Champaign, Urbana, 2020).
[48]I. G. Dors and C. G. Parigger, "Computational fluid-dynamic model of laser-induced breakdown in air," Appl. Opt. **42**, 5978–5985 (2003).
[49]C. Dumitrache and A. P. Yalin, "Gas dynamics and vorticity generation in laser-induced breakdown of air," Opt. Express **28**, 5835–5850 (2020).
[50]M. Nishihara, J. B. Freund, N. G. Glumac, and G. S. Elliott, "Influence of mode-beating pulse on laser-induced plasma," J. Phys. D: Appl. Phys. **51**, 135601 (2018).
[51]P. Sprangle, E. Esarey, and A. Ting, "Nonlinear theory of intense laser-plasma interactions," Phys. Rev. Lett. **64**, 2011 (1990).
[52]P. Mora and T. M. Antonsen, Jr., "Kinetic modeling of intense, short laser pulses propagating in tenuous plasmas," Phys. Plasmas **4**, 217–229 (1997).
[53]J. H. Cooley, "Modeling laser pulse evolution in ionizing gas and plasma with application to laser wakefield acceleration," Ph.D. thesis (University of Maryland, 2004).
[54]S. Carusotto and C. Strati, "Incoherent and coherent pulses and multiphoton absorption probability," Il Nuovo Cimento B **15**, 159–180 (1973).
[55]C. Lecompte, G. Mainfray, C. Manus, and F. Sanchez, "Experimental demonstration of laser temporal coherence effects on multiphoton ionization processes," Phys. Rev. Lett. **32**, 265 (1974).

30 August 2023 12:22:34

Published under an exclusive license by AIP Publishing

[56]A. Alcock, C. Demichelis, and M. Richardson, "Breakdown and self-focusing effects in gases produced by means of a single-mode ruby laser," IEEE J. Quantum Electron. **6**, 622–629 (1970).
[57]L. R. Evans and C. G. Morgan, "Lens aberration effects in optical-frequency breakdown of gases," Phys. Rev. Lett. **22**, 1099 (1969).
[58]L. Y. Margolin, "Generation of periodic inhomogeneities in optical breakdown by a Bessel laser beam," Quantum. Elec. **29**, 246 (1999).
[59]P. Kaw, "Nonlinear effects of laser propagation in dense plasmas," Appl. Phys. Lett. **15**, 16–18 (1969).
[60]P. A. Gnoffo, R. N. Gupta, and J. L. Shinn, "Conservation equations and physical models for hypersonic air flows in thermal and chemical nonequilibrium," NASA Technical Paper 2867 (1989).
[61]C. G. Morgan, "Some aspects of laser-produced plasmas," Plasma Phys. Controlled Fusion **26**(12A), 1367 (1984).
[62]N. Kroll and K. M. Watson, "Theoretical study of ionization of air by intense laser pulses," Phys. Rev. A **5**, 1883 (1972).
[63]D. R. Skinner and R. E. Whitcher, "Measurement of the radius of a high-power laser beam near the focus of a lens," J. Phys. E: Sci. Instrum. **5**, 237 (1972).
[64]N. Tsuda and J. Yamada, "Observation of forward breakdown mechanism in high-pressure argon plasma produced by irradiation by an excimer laser," J. Appl. Phys. **81**, 582–596 (1997).
[65]N. Tsuda and J. Yamada, "Mechanism of forward development of a plasma produced by an excimer laser in high-pressure argon gases," J. Appl. Phys. **87**, 2122–2126 (2000).
[66]S. Yalçin, D. R. Crosley, G. P. Smith, and G. W. Faris, "Influence of ambient conditions on the laser air spark," Appl. Phys. B **68**, 121–130 (1999).
[67]H. El-Rabii, S. B. Victorov, and A. P. Yalin, "Properties of an air plasma generated by ultraviolet nanosecond laser pulses," J. Phys. D: Appl. Phys. **42**, 075203 (2009).
[68]C. Limbach and R. Miles, "Simultaneous temperature, density and velocity measurements in laser-generated plasmas by Rayleigh and filtered Rayleigh scattering," in *52nd Aerospace Sciences Meeting* (AIAA, 2014), p. 0143.
[69]C. Dumitrache, C. M. Limbach, and A. P. Yalin, "Threshold characteristics of ultraviolet and near infrared nanosecond laser induced plasmas," Phys. Plasmas **23**, 093515 (2016).
[70]N. Glumac, G. Elliott, and M. Boguszko, "Temporal and spatial evolution of a laser spark in air," AIAA J. **43**, 1984–1994 (2005).

30 August 2023 12:22:34

Published under an exclusive license by AIP Publishing